

Article

# Experimental and Analytical Study of Directional Isothermal Fatigue in Additively Manufactured Ti-TiB Metal Matrix Composites

Thevika Balakumar , Reza A. Riahi and Afsaneh Edrisy

Department of Mechanical, Automotive & Materials Engineering, University of Windsor, Windsor, ON N9B 3P4, Canada; ariahi@uwindsor.ca (R.A.R.); edrisy@uwindsor.ca (A.E.)

\* Correspondence: balakumt@uwindsor.ca

**Abstract:** Additive manufacturing (AM) techniques are widely investigated for the cost-effective use of titanium (Ti) alloys in various aerospace applications. One of the AM techniques developed for such applications is plasma transferred arc solid free-form fabrication (PTA-SFFF). Materials manufactured through AM techniques often exhibit anisotropies in mechanical properties due to the layer-by-layer material build. In this regard, the present study investigates the isothermal directional fatigue of a Ti-TiB metal matrix composite (MMC) manufactured by PTA-SFFF. This investigation includes a rotating beam fatigue test in the fully reversed condition (stress ratio,  $R = -1$ ), electron microscopy, and calculations for fatigue life predictions using Paris' and modified Paris' equations. The fatigue experiments were performed at 350 °C using specimen with the test axis oriented diagonally (45°) and parallel (90°) to the AM builds directions. The fatigue values from the current experiments along with literature data find that the Ti MMC manufactured via PTA-SFFF exhibit fatigue anisotropy reporting highest strength in 90° and lowest in perpendicular (0°) AM build directions. Furthermore, calculations were performed to evaluate the optimum values of the stress intensity modification factor ( $\lambda$ ) for fatigue life prediction in 0°, 45°, and 90° AM build directions. It was found that for the specimens with 45°, and 90° AM build directions, the computed intensity modification factors were very similar. This suggests that the initial fatigue crack characteristics such as location, shape, and size were similar in both 45°, and 90° AM build directions. However, in 0° AM build direction, the computed stress intensity modification factor was different from that of the 45°, and 90° AM build directions. This indicates that the fatigue crack initiation at 0° AM build direction is different compared to the other two directions considered in this study. Moreover, the quality of fatigue life prediction was assessed by calculating  $R^2$  values for both Paris and modified Paris predictions. Using the  $R^2$  values, it was found that the fatigue life predictions made by the modified Paris equation resulted in improved prediction accuracy for all three builds, and the percentage improvement ranged from 30% to 60%. Additionally, electron microscopy investigations of 0°, 45°, and 90° AM build specimens revealed extensive damage to the TiB particle compared to the Ti matrix as well as frequent TiB clusters in all three AM build directions. These observations suggest that the spread of these TiB clusters plays a role in the fatigue anisotropy of Ti-TiB MMCs.

**Keywords:** additive manufacturing; directional fatigue; isothermal fatigue; fatigue anisotropy; Ti-TiB MMC; Paris equation; modified Paris equation



**Citation:** Balakumar, T.; Riahi, R.A.; Edrisy, A. Experimental and Analytical Study of Directional Isothermal Fatigue in Additively Manufactured Ti-TiB Metal Matrix Composites. *Metals* **2024**, *14*, 408. <https://doi.org/10.3390/met14040408>

Academic Editor: Giovanni Meneghetti

Received: 5 March 2024

Revised: 25 March 2024

Accepted: 28 March 2024

Published: 29 March 2024



**Copyright:** © 2024 by the authors. Licensee MDPI, Basel, Switzerland. This article is an open access article distributed under the terms and conditions of the Creative Commons Attribution (CC BY) license (<https://creativecommons.org/licenses/by/4.0/>).

## 1. Introduction

The utilization of additive manufacturing (AM) in aerospace component manufacturing and repair is on the rise due to its material and cost-saving capabilities, without compromising the mechanical properties of the components. According to the European patent office publication [1], aerospace is the largest field among the transportation industry that uses AM to manufacture lightweight components, thereby aiding in the reduction

of weight, fuel consumption, and emissions. In this regard, titanium (Ti) alloys are often selected as candidate materials in such applications due to their high specific strength and good corrosion resistance at elevated temperatures [2,3]. When considering Ti alloy use in the aerospace industry, they are often utilized in constructing airframe parts and gas turbine engines parts [2–5]. In order to meet the present-day demand for improved mechanical properties and to reduce the production costs of Ti alloys, research has been conducted on various Ti MMCs [6–10]. Reinforcements for MMCs are generally introduced in the form of fibers (continuous or discontinuous) or particles [11,12]. When compared to fiber-reinforced composites, particle-reinforced composites show potential in displaying isotropic properties. The widely used particle reinforcements in MMCs include borides, carbides, nitrides, and graphene [13–15]. In this regard, it was reported in [16–18] that Ti MMCs with TiB particle reinforcements show great promise as they exhibit a high elastic modulus (approximately 450–550 GPa) and thermal stability.

The critical studies in [19–22] present a number of AM techniques available for Ti alloys and composites. The research in [19] identifies laser powder bed fusion (L-PBF), laser direct energy deposition (L-DED), and electron beam powder bed fusion (E-PBF) as the AM techniques that can provide near-fully dense commercially pure Ti alloy components. In [20], it is reported that powder bed fusion (PBF) and directed energy deposition (DED) methods are the two widely used forms of AM techniques for metals and alloys, and it critically analyzes the PBF process for Ti-6Al-4V alloys. Furthermore, the research presented in [21] analyzes powder feed AM techniques such as L-PBF and E-PBF for Ti-6Al-4V with the focus on the reusability of powders. It also highlights challenges such as the roughening of particles and compositional changes that occur during powder reuse. Moreover, the study in [22] presents the use of selective laser melting (SLM) for Ti MMC manufacturing. The studies presented in [19–22] also analyze the advantages of AM methods over conventional manufacturing methods for Ti alloys and composites. These advantages include very high cooling rates involved in AM processes, which result in the formation of useful metastable phases and microstructures, thereby enhancing the material's strength and the reusability of metal powders. However, these AM techniques face challenges when manufacturing reliable products with isotropic properties due to non-equilibrium cooling rates and various process parameters such as deposition rate, scanning velocity, and additive layer thickness.

One of the disadvantages of considering AM over conventional manufacturing processes is that the materials manufactured through AM techniques often exhibit anisotropic properties, showing varying mechanical properties, such as tensile, compressive, and fatigue strengths, along different AM build directions due to their layer-by-layer material build technique and the microstructure and defects associated with it [23–25]. In this context, Ti-6Al-4V alloys manufactured through SLM and DED were often experimentally studied [26–29]. All three of these studies reported the anisotropic fatigue strength of Ti-6Al-4V with respect to AM build directions. Further, they reported higher fatigue strengths when the test axes were along  $0^\circ$  [26,27] and  $90^\circ$  [28,29] to the AM direction.

The fatigue study in [26] investigated the directional fatigue strength of SLM Ti-6Al-4V. It utilized machined test specimens from SLM rods, testing them at room temperature on an electromagnetic resonance fatigue machine (QBG-25). The fatigue anisotropy observed in that study was attributed to the crystallographic texture and columnar grains in the SLM material build. In [27], AM Ti-6Al-4V samples built via SLM were tested for directional fatigue strength on an MTS 810 fatigue testing machine at room temperature. In that study, the observed anisotropic fatigue strengths at  $0^\circ$  and  $90^\circ$  angles to the AM directions were attributed mainly to the weak inter layer bonding. In [28], a directional fatigue study was carried out using both machined and as-built SLM Ti-6Al-4V samples on an MTS load frame at room temperature. The study suggested that aspects associated with the SLM process, such as porosity, microstructure, and surface roughness, could have contributed to the observed fatigue anisotropy. In [29], the directional fatigue strength of Ti-6Al-4V manufactured by the DED process was studied. In that work, machined test specimens

from a DED block were tested on an Instron (model 8801) hydraulic servo fatigue tester at room temperature. The study attributed the crystallographic texture and alpha colonies with directional characteristics to fatigue anisotropy.

In the present work, the directional isothermal fatigue of Ti-TiB MMCs manufactured by plasma transferred arc solid free-form fabrication (PTA-SFFF) [30] was investigated. According to [30], the PTA-SFFF technique utilizes two DC power supplies, each capable of supplying up to 350 amperes to operate two PTA torches, enabling the deposition of material at rates of up to 35 pounds per hour in an inert argon gas deposition chamber. In the current study, the fatigue of Ti-TiB MMCs was investigated at 350 °C in three additive manufacturing (AM) build orientations: 0° (where the test axis is parallel to the AM direction), 45° (where the test axis is at a 45° angle to the AM direction), and 90° (where the test axis is perpendicular to the AM direction). Among these three AM directions, experimental data on the 45° and 90° AM build directions were collected in the present study. Data on the 0° AM build direction at 350 °C were extracted from the current authors' previous experimental work reported in [31]. Further, the fatigue data for the current work were collected using a rotating beam fatigue (RBF) tester following the experimental setup described in [31]. Moreover, to investigate the influence of TiB on crack initiations, propagations, and the overall directional fatigue strength of Ti-TiB MMCs, electron microscopy images were collected from polished as well as fatigue fractured specimens. In addition to the current fatigue and electron microscopy experimental work, an analytical investigation on the fatigue life predictability of the modified Paris equation described in [31] was tested against the general Paris equation using current and literature [31] experimental data.

The above-described directional isothermal fatigue investigation of AM Ti-TiB MMCs is further detailed in the remainder of this manuscript under Sections 2–4. In Section 2, specimen orientations, current experimental results on isothermal fatigue in the 45° and 90° AM build directions, and electron microscopy images are provided. In Section 3, the experimental findings on directional fatigue (in the 0°, 45°, and 90° AM build directions) and Ti-TiB MMC fracture characteristics at 350° are analyzed. This section also presents fatigue calculations associated with the current experimental data using Paris and modified Paris equations. Finally, the findings of the current experimental and analytical work are presented in Section 4.

## 2. Specimen Orientations and Experimental Results

In the current work, isothermal fatigue was studied in three AM build directions, and they are schematically illustrated in Figure 1a. The specimens for the fatigue tests were machined out from a 95 × 31 × 190 mm PTA-SFFF Ti-TiB MMC, following the ASTM E606/E606M standard. These specimens have circular cross sections, featuring hour-glass-shaped test sections with a minimum diameter of 4.76 mm at the mid test section. These specimens were then mechanically polished to have an average surface roughness (Ra) of 0.2 µm or less. The process involved successive polishing steps using P280, P400, P800, P1200, and P4000 SiC polishing papers (Buehler Ltd., Lake Bluff, IL, USA), followed by a final polishing step utilizing a 1-micron polycrystalline diamond suspension on a micro cloth. Subsequently, these samples were ultrasonically cleaned in acetone before being secured in the RBF HT 200 tester (Systems Integrators LLC, Glendale, CA, USA), shown in Figure 1b. The fatigue tester was configured for fully reversed fatigue loading conditions, subjecting the test specimen to both tension and compression within a single cycle, while maintaining a stress ratio of  $R = -1$ . The main components of the RBF tester, including the specimen-collet assembly, heating unit, temperature controller, poise weight, and cycle counter, are labeled in Figure 1b.

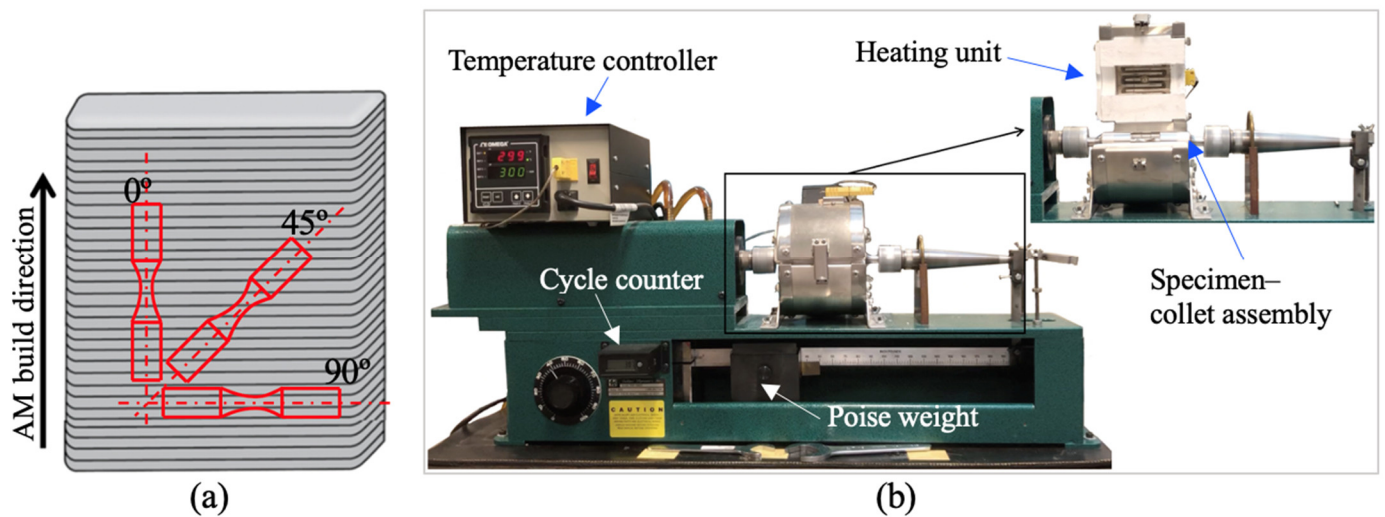


**Figure 1.** (a) Schematic of three different fatigue specimen axis orientations ( $0^\circ$ ,  $45^\circ$ , and  $90^\circ$ ) with respect to the AM build direction that were considered in the present study. (b) RBF HT 200 tester and its main components.

The current experimental fatigue data for AM Ti-TiB MMCs at  $350^\circ\text{C}$  in the  $45^\circ$  and  $90^\circ$  AM build directions along with fatigue data from the literature [31] in the  $0^\circ$  AM build direction at  $350^\circ\text{C}$  are presented in Figure 2 as a plot of stress amplitude ( $\sigma$ ) against the number of cycles to failure ( $N_f$ ).

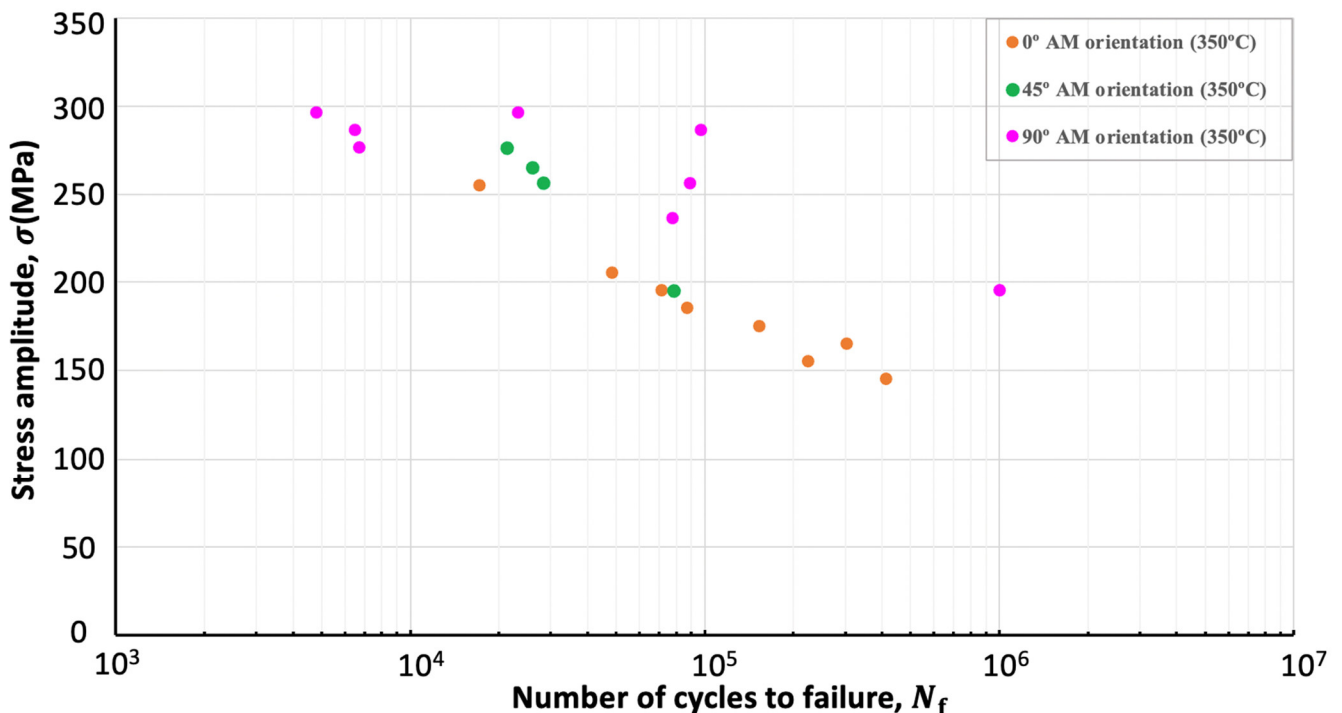


**Figure 2.** Stress amplitude ( $\sigma$ ) vs. the number of cycles to failure ( $N_f$ ) plots for the isothermal fatigue strengths of AM Ti-TiB MMCs in the  $0^\circ$ ,  $45^\circ$ , and  $90^\circ$  AM build directions at  $350^\circ\text{C}$ . Here the current experimental data is denoted by green and pink circles while the data from [31] is denoted by orange circles.

The electron microscopy images collected from the fractured fatigue specimens as well as from polished and etched specimens with  $0^\circ$ ,  $45^\circ$ , and  $90^\circ$  AM build directions are given in Figures 3–6. The specimens that were polished and etched were cut in such

a manner that representative cross sections of the fatigue specimens with 0°, 45°, and 90° AM builds could be studied. The low-magnification (28×) back-scattered electron (BSE) images in Figure 3 show the complete fracture surfaces of fatigue specimens with 45° (Figure 3a) and 90° (Figure 3b) AM build orientations. The arrows in these images point to multiple crack paths during fatigue failure. Within the magnification range of 600–8000×, the high-magnification BSE images in Figure 4 depict fracture characteristics, such as matrix cleavage, blocked pores, and striations, observed in samples with 45° and 90° AM orientations. The TiB particles detected through energy-dispersive spectroscopy (EDS) are labeled in these images. Additionally, Figure 5 comprises a BSE image taken along the peripheral surface of a fractured fatigue specimen showing extensive cracks in TiB, which were identified through EDS.

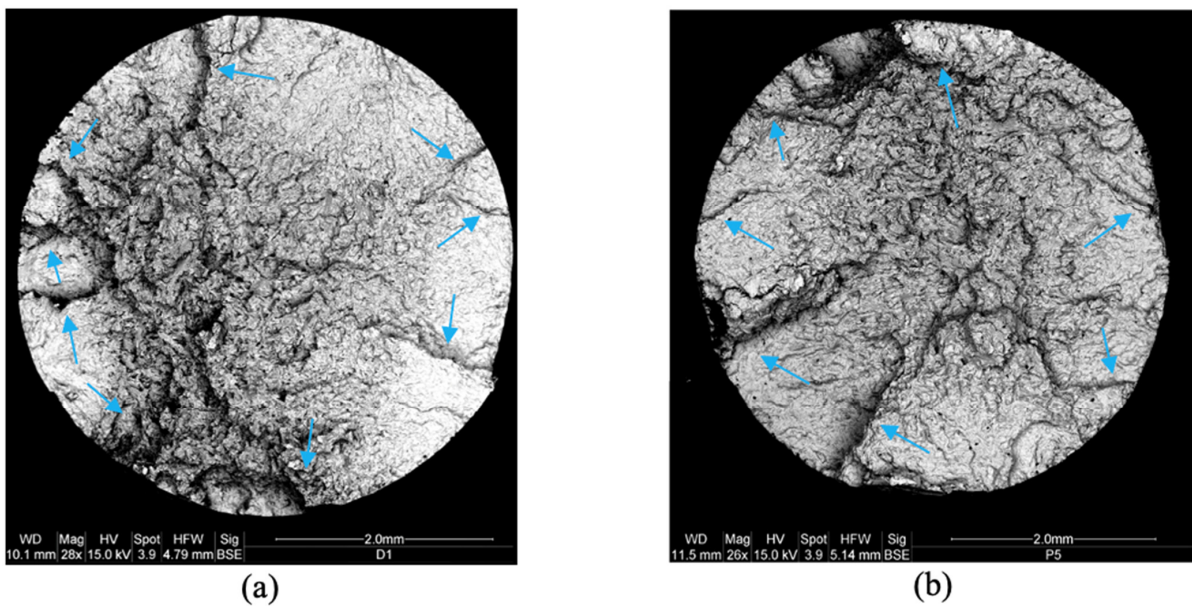


**Figure 3.** BSE images of (a) a 45° AM build direction specimen fractured at the applied stress of  $\sigma = 256.5$  MPa and at 350 °C; (b) a 90° AM build direction specimen fractured at the applied stress of  $\sigma = 296.5$  MPa and at 350 °C.

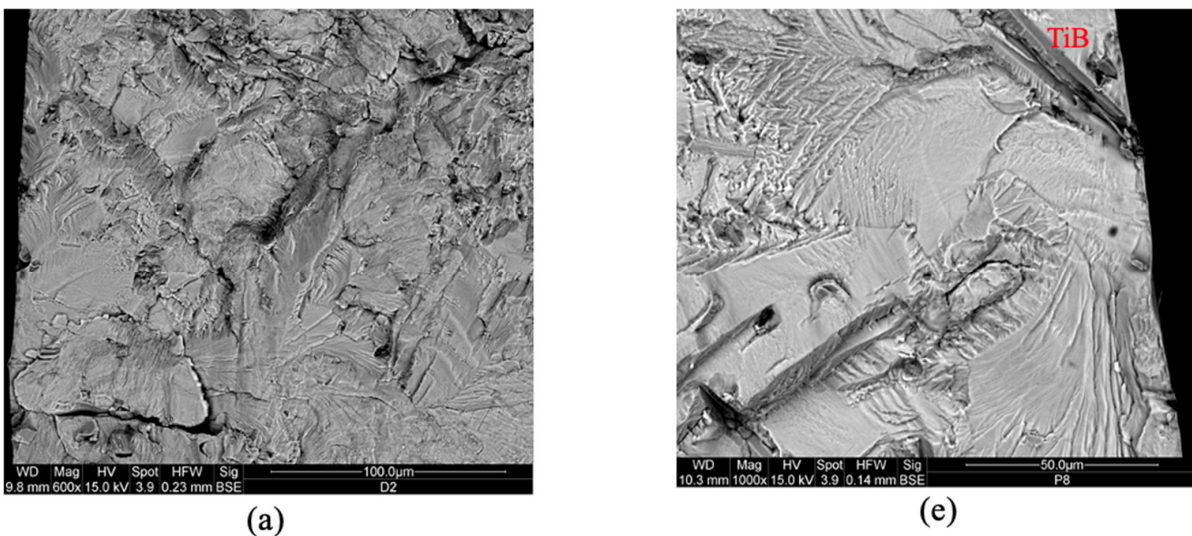


**Figure 4.** Cont.

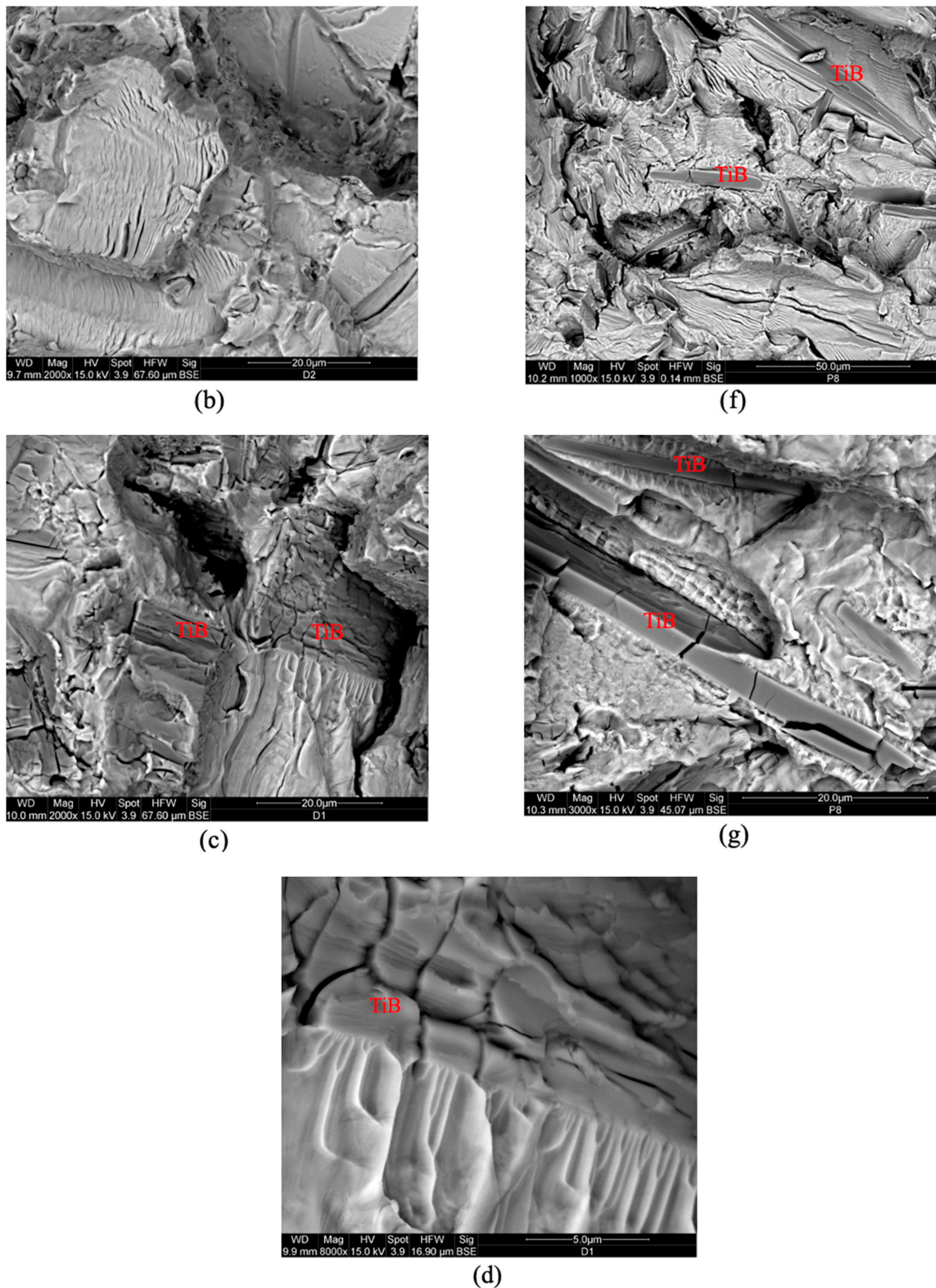


**Figure 4.** BSE images of 45° additive build orientation samples that show fracture characteristics such as (a) cleavage in alpha Ti matrix; (b) region of striations in alpha Ti matrix; (c) fractured TiB particles surrounded by features of blocked pores during fracture; (d) an enlarged portion of (c) showing striations in broken TiB particle. The following are BSE images of 90° AM orientation samples that show fracture features such as (e) alpha Ti matrix cleavage; (f) striations in alpha Ti matrix; (g) fractured TiB particles surrounded by features of blocked pores during fracture.

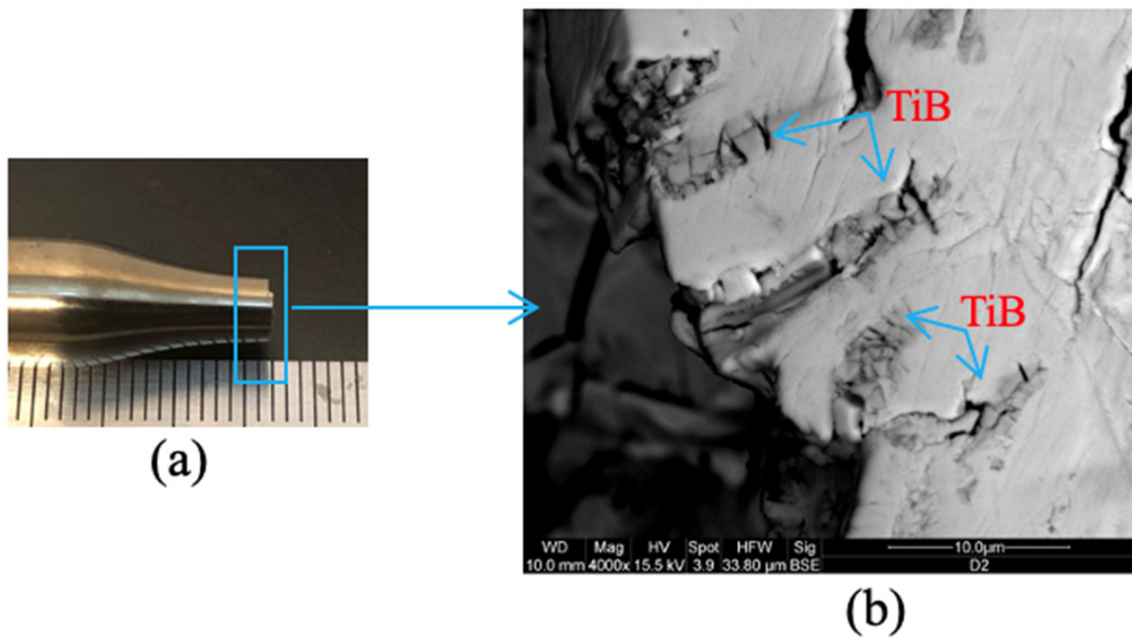


**Figure 5.** (a) One half of a fatigue-fractured test specimen. (b) BSE image of the peripheral surface of the fractured fatigue specimen shown in (a).

Since the TiB particles showed significant fracture, samples with  $0^\circ$ ,  $45^\circ$ , and  $90^\circ$  AM build orientations were polished, etched, and observed under an electron microscope to find how these particles are distributed in the Ti matrix. The optical microscopy images, captured at a magnification of  $600\times$  and presented in Figure 6a–d, show the distribution of TiB particles and the alpha-Ti matrix–grain boundaries (GB) observed in samples with  $0^\circ$ ,  $45^\circ$ , and  $90^\circ$  AM build orientations. More optical microscopy images in Figure 6e–g, taken at a lower magnification of  $40\times$ , show the TiB clusters across the same three AM orientations. These clusters are labeled and indicated by arrows.

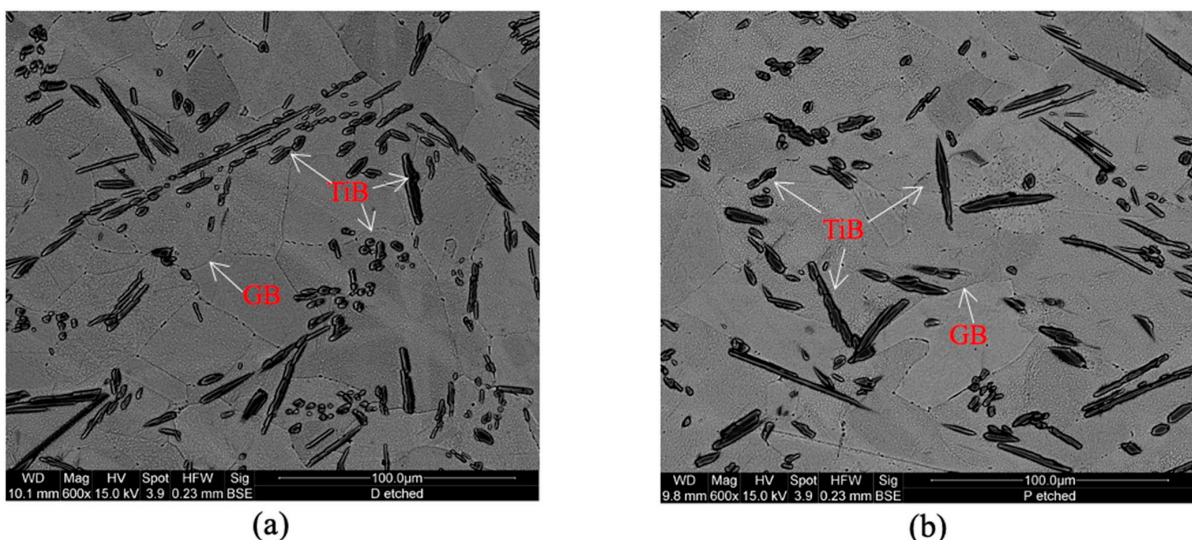


**Figure 6.** Cont.

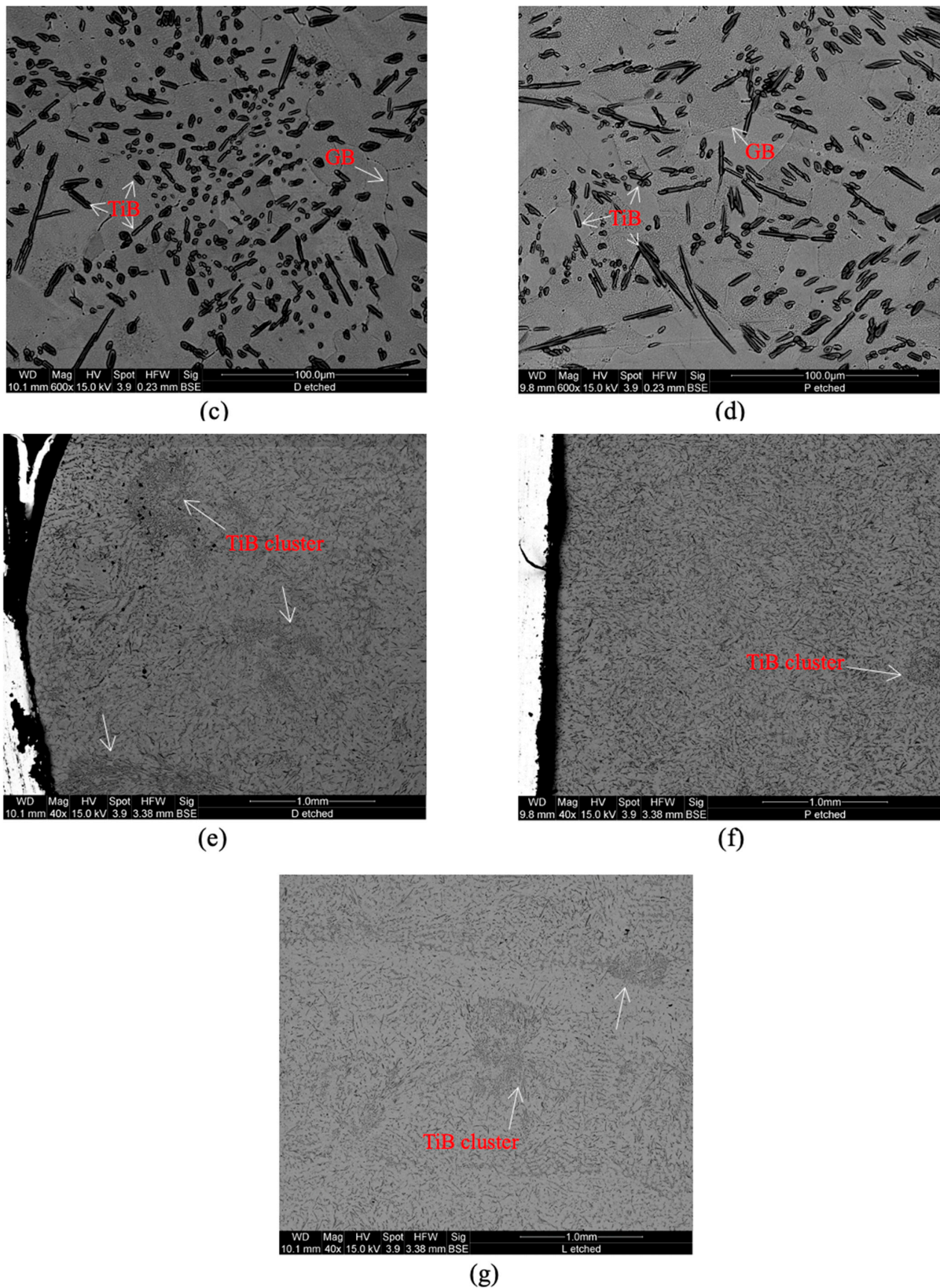


**Figure 6.** BSE images showing random distribution TiB particles in (a) the 45° and (b) the 90° AM build specimens. BSE images showing occasional cluster of TiB in (c) the 45° and (d) the 90° AM build specimens. Low-magnification BSE images showing the general spread of TiB particles and TiB clusters in (e) the 45°, (f) the 90°, and (g) the 0° AM build specimens.

### 3. Analysis

The isothermal fatigue plots in Figure 2 show that Ti-TiB MMCs manufactured by PTA-SFFF exhibit fatigue anisotropy with the highest strength in 90°, moderate in 45°, and the lowest in 0° AM build orientations. Similar fatigue anisotropic results were observed in [17,18], in which the directional fatigue strengths of AM Ti-6Al-4V at room temperature were studied. Even though the fatigue plots in Figure 2 show fatigue anisotropy, specimens of all three AM build orientations exhibited similar fatigue fractures, as shown in Figures 3 and 4 for 45° and 90° AM build specimens. Similar images for the 0° AM build specimen can be found in [19].

Further, the 45° and 90° AM build specimens exhibited more significant cleavage on the fractured surfaces compared to the 0° AM build specimen. Other fracture features such as dense striations in the alpha matrix (Figure 4b,f) and broken TiB particles were observed in all three AM build direction specimens. These dominant fracture features are given in Figure 4 for 45° and 90° AM build specimens and can be found in [19] for 0° AM build specimens. Moreover, TiB particles in all the tested specimens generally showed no striation marks when they were observed under an SEM. However, it can be seen from Figure 4d that the higher magnification BSE image shows slight signs of striations in a TiB particle that is heavily surrounded by frill like features. This observation suggests that when the TiB particle blocks the moving pores, there is also a discernible degree of plastic deformation during fatigue.

When considering the impact of TiB particles on the fatigue fracture of the tested AM alpha Ti alloy containing TiB particles, it is evident from Figure 5b that the TiB particles undergo significant fracture in comparison to the alpha Ti matrix. Further, the SEM images in Figure 6 reveal several characteristics of TiB particles: (i) There is a slight preference for the TiB particles to sit near the grain boundaries of the alpha Ti grains (Figure 6a,b). (ii) There is a preference for them to be in and around alpha Ti grains with a particular texture (Figure 6a–d). (iii) There is clustering in the alpha Ti matrix (Figure 6e–g). These microscopic observations, along with those presented in Figures 3 and 5b, showing major surface crack propagations and significant fractures in TiB particles, respectively, suggest that the distribution of TiB particles is a factor in determining the isothermal fatigue life of AM Ti-TiB MMCs. For instance, when a surface crack initiates at a site with a cluster of TiB particles, it will propagate easily, as they exhibit significant fracture compared to the alpha Ti matrix. Moreover, it can be seen from Figure 6g that, compared to the TiB particle distributions observed in materials built with 45° and 90° AM build orientations, as shown in Figure 6e and f, respectively, the particle distribution in the 0° AM build material exhibits a distinct and layered pattern of TiB particles. From this observation of TiB particles in the alpha Ti matrix along with their significant fracture during fatigue, this study suggests that the distribution of TiB particles during PTA SFFF contributed to the observed fatigue anisotropy as well as for the lowest fatigue along the 0° AM build compared to those at 45° and 90°.

In addition to the experimental fatigue and microscopy investigation presented in the present work, fatigue life calculations were carried out to evaluate the predictability of the modified Paris equation presented in [19] by the authors of this manuscript. In this regard, the directional isothermal fatigue of AM Ti-TiB MMCs was calculated using the Paris (Equation (1)) and modified Paris equations (Equation (2)).

$$N_{\text{FP}} = \frac{a_f^{1-\frac{n}{2}} - a_i^{1-\frac{n}{2}}}{(1-\frac{n}{2})\beta\lambda^n(\Delta\sigma)^n\pi^{\frac{n}{2}}} \quad (1)$$

$$N_{\text{fM}} = \frac{\left(\frac{a_f}{\mu}\right)^{1-\frac{n}{2}} - a_i^{1-\frac{n}{2}}}{(1-\frac{n}{2})\beta\lambda^n(\Delta\sigma)^n\pi^{\frac{n}{2}}} \quad (2)$$

In the above equations,  $N_{fP}$  and  $N_{fM}$  denote the calculated number of cycles to failure using Equations (1) and (2), respectively;  $\lambda$  denotes the stress intensity modification factor;  $\beta$  and  $n$  are material constants (that can found in the literature);  $a_i$  and  $a_f$  refer to the initial and final lengths of the surface crack;  $\Delta\sigma$  is applied stress; and  $\mu$  refers to the number of major surface cracks that have propagated. As described in [19], the values of  $\lambda$  for the best prediction by Equations (1) and (2), denoted, respectively, by  $\lambda_P^*$  and  $\lambda_M^*$ , can be found through least square error minimization, and their closed form expressions are, respectively, given by Equations (3) and (4).

$$\lambda_P^* = \left[ \frac{\sum_{j=1}^z \left( \frac{\gamma_{jP}}{\delta_j} \right)^2}{\sum_{j=1}^z \left( \frac{\gamma_{jP}}{\delta_j} \right) \cdot N_{fj}^{Exp}} \right]^{\frac{1}{n}} \tag{3}$$

$$\lambda_M^* = \left[ \frac{\sum_{j=1}^z \left( \frac{\gamma_{jM}}{\delta_j} \right)^2}{\sum_{j=1}^z \left( \frac{\gamma_{jM}}{\delta_j} \right) \cdot N_{fj}^{Exp}} \right]^{\frac{1}{n}} \tag{4}$$

where

$$\gamma_{jP} = a_{fj}^{1-\frac{n}{2}} - a_{ij}^{1-\frac{n}{2}} \tag{5}$$

$$\delta_j = \left( 1 - \frac{n}{2} \right) \beta \pi^{\frac{n}{2}} (\Delta\sigma_j)^n \tag{6}$$

$$\gamma_{jM} = \left( \frac{a_{fj}}{\mu_j} \right)^{1-\frac{n}{2}} - a_{ij}^{1-\frac{n}{2}} \tag{7}$$

for  $j$  number of experiments.

The evaluation of  $\lambda_P^*$  and  $\lambda_M^*$  in  $0^\circ$ ,  $45^\circ$ , and  $90^\circ$  AM build orientations using Equations (1) and (2) are illustrated in Figure 7, and their values are tabulated in Table 1.

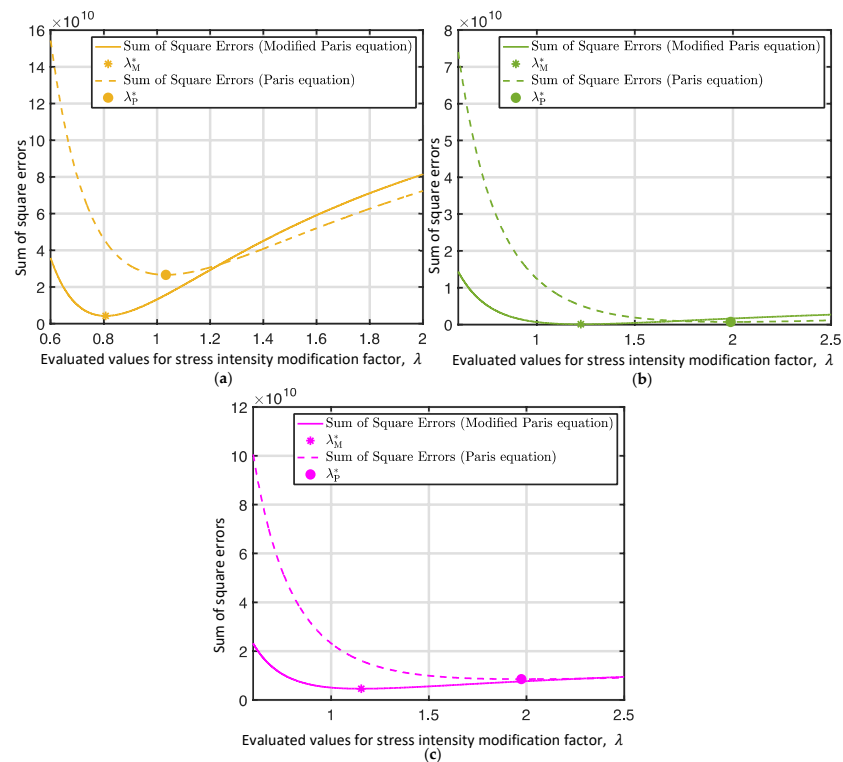


**Figure 7.** Plots for sum of square errors for calculations using the Paris equation (1) and the modified Paris equation (2) are presented for (a) the  $0^\circ$  (b) the  $45^\circ$ , and (c) the  $90^\circ$  AM build orientations.

**Table 1.** Evaluated optimum stress intensity modification factors for the 0°, 45°, and 90° AM build orientations.

Specimen AM Build Orientation	$\lambda_P^*$ for Equation (1)	$\lambda_M^*$ for Equation (2)
0°	1.0333	0.8069
45°	1.9880	1.2247
90°	1.9737	1.1537

It can be noted from Table 1 that the evaluated values for  $\lambda_P^*$  and  $\lambda_M^*$  for 45° and 90° AM build directions are almost the same and higher than that for 0°. Since the stress intensity modification factor,  $\lambda$ , depends on the initial crack characteristics, such as location, shape, and size, similar values of  $\lambda_P^*$  and  $\lambda_M^*$  suggest that both 0° and 45° AM build specimens had similar crack initiation characteristics.

Moreover, using the values listed Table 1 for the modification factors for the 0°, 45°, and 90° AM build orientations, and by taking the values for  $\beta = 2 \times 10^{-8}$  and  $n = 1.19$ , fatigue calculations were performed using Equations (1) and (2), and they are illustrated as S–N plots in Figure 8 along with experimental data from the current work as well as from the work reported in [19]. Furthermore, according to the description for  $\lambda$  given in [19], the initial surface crack length,  $a$ , and the value of  $\lambda$  are inversely proportional. Hence, the lower values for  $\lambda_P^*$  and  $\lambda_M^*$  in Table 1 suggest larger surface crack initiations and lower fatigue values. This is evidenced by the smaller  $\lambda_P^*$  and  $\lambda_M^*$  values (Table 1) and lower fatigue strength (Figure 2) observed in the 0° AM build direction compared to that in the 45° and 90° orientations. Further, the quality of these fatigue life calculations by Equations (1) and (2) were evaluated in terms of  $R^2$  and are tabulated in Table 2. It can be noted from Table 2 that the  $R^2$  values evaluated in relation to Equation (2) are superior to the ones for Equation (1). This finding suggests that the modified Paris equation in Equation (2) makes a more accurate fatigue life prediction than Equation (1).

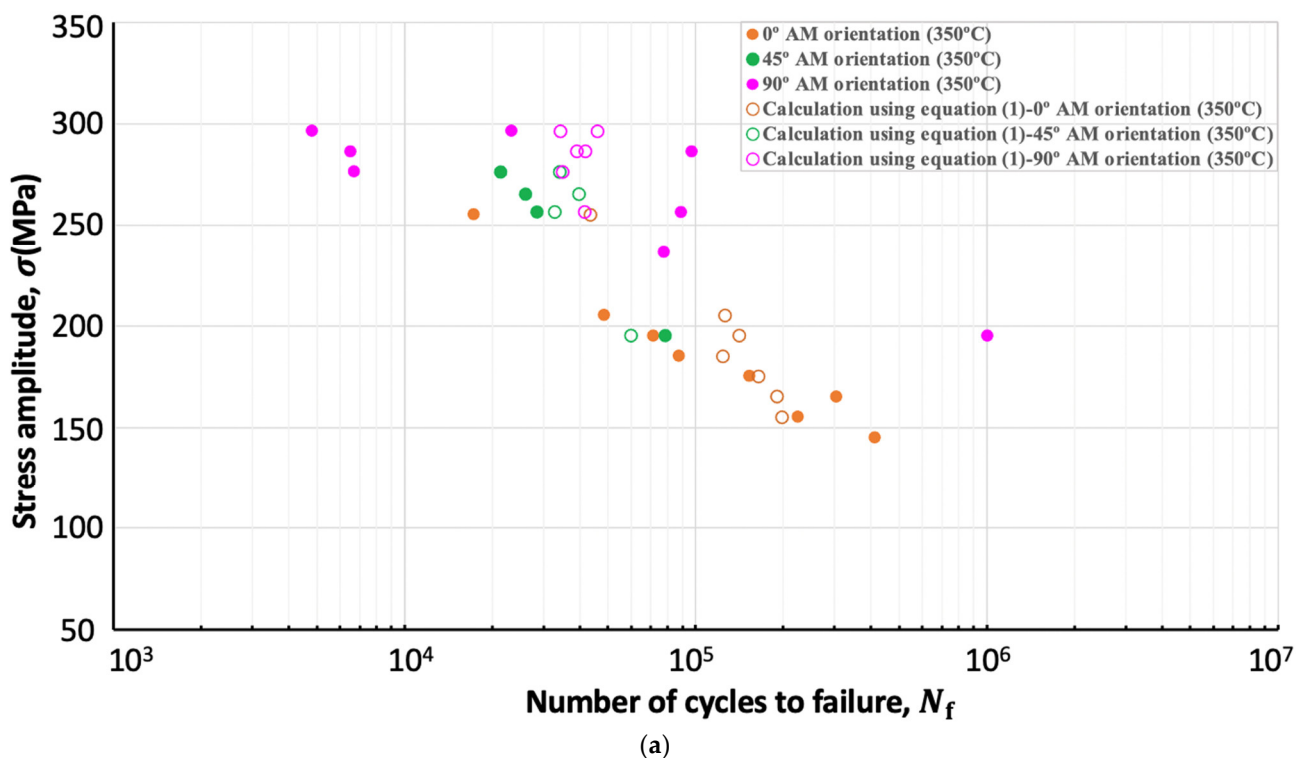
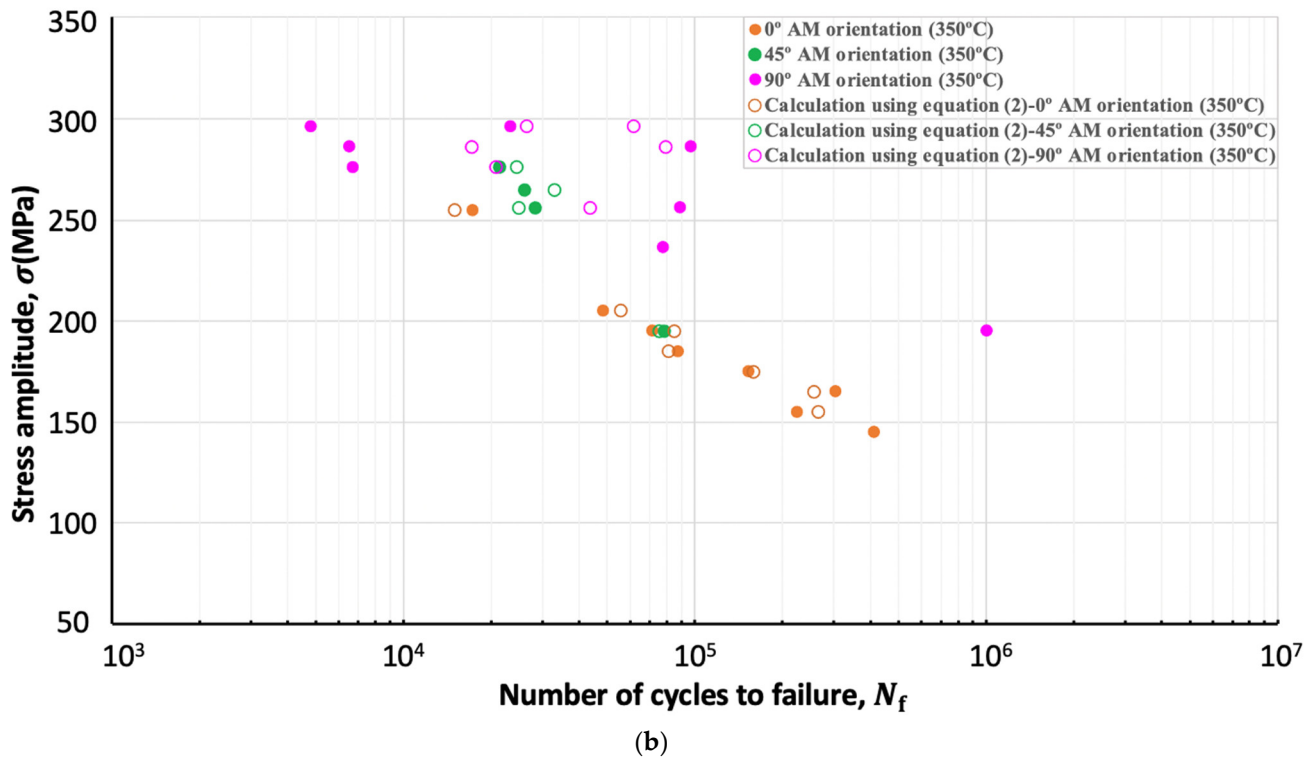


Figure 8. Cont.



**Figure 8.** The plots of stress amplitude ( $\sigma$ ) versus the number of cycles to failure ( $N_f$ ) for specimens with  $0^\circ$ ,  $45^\circ$ , and  $90^\circ$  AM build orientations showing both experimental (filled circles, the current experimental data is denoted by green and pink circles while the data from [31] is denoted by orange circles.) and calculated (clear circles) data points: (a) contains calculated data using the Paris Equation (1); (b) contains calculated data using the modified Paris Equation (2).

**Table 2.** Evaluated  $R^2$  values for the fatigue life of specimens with the  $0^\circ$ ,  $45^\circ$  and  $90^\circ$  AM build orientations calculated using Paris equation (1) and the modified Paris Equation (2).

Specimen AM Build Orientation	$R^2$ for Fatigue Life Calculation Using Equation (1)	$R^2$ for Fatigue Life Calculation Using Equation (2)
$0^\circ$	0.34	0.93
$45^\circ$	0.67	0.96
$90^\circ$	0.09	0.51

#### 4. Conclusions

This study finds that the Ti-TiB MMC manufactured by plasma transferred arc solid free-form fabrication (PTA-SFFF) shows fatigue anisotropy. Among the three AM orientations considered in the present study,  $90^\circ$  AM build orientations exhibited better fatigue strength compared to those with  $0^\circ$  and  $45^\circ$  orientations.

Electron microscopy images obtained from the fractured specimen surfaces reveal that the final fracture in all three AM build directions occurred due to several large surface crack propagations. Also, these images show considerable cracks in TiB compared to the Ti matrix. Further, the microscopy images obtained from the polished and etched specimen show frequent TiB clusters in in all three AM build directions. However, the  $0^\circ$  specimen exhibited a significantly different variation in TiB distribution, possibly between each AM build layer. These images also reveal that TiB particles are preferably distributed along the matrix–grain boundaries.

The fatigue calculations performed in the present work find that the modified Paris equation, which incorporates the contribution from the number of large surface crack propagations, accurately predicts the fatigue life of Ti-TiB MMCs manufactured via PTA-SFFF

in all AM build directions. This finding suggests that this modified Paris equation can be used for any AM material that exhibits a significant number of surface crack propagations. Moreover, the lowest value calculated for the stress intensity modification factor for the 0° AM build orientation supports the lowest experimental fatigue recordings and significant TiB clusters in microscopy images. Furthermore, almost the same values of the stress intensity modification factor were calculated for the 45° and 90° AM build directions. This finding suggests similar crack initiation characteristics in these AM build directions.

With regard to the crack initiation sites, no specific metallurgical factors—such as strain localization regions, also known as slip bands [32]; grain size and shape; [33] and grain orientation with respect to the basal and prismatic slip planes [34]—were identified in this work. Hence, advanced image analysis that can reveal atomic-level characteristics is required to investigate crack initiation. Furthermore, to investigate crack propagation behavior under the isothermal fatigue of Ti-TiB MMCs, more experiments are required.

**Author Contributions:** Conceptualization, T.B.; Methodology, T.B.; Validation, T.B. and R.A.R.; Formal analysis, T.B.; Investigation, T.B.; Data curation, T.B.; Writing—original draft, T.B.; Writing—review and editing, T.B. and R.A.R.; Visualization, T.B.; Supervision, R.A.R. and A.E.; Project administration, A.E.; Funding acquisition, A.E. All authors have read and agreed to the published version of the manuscript.

**Funding:** This research received no external funding.

**Data Availability Statement:** The raw data supporting the conclusions of this article will be made available by the authors on request.

**Acknowledgments:** The authors would like to thank the reviewers for carefully reading this manuscript and for providing their valuable comments and suggestions which contributed to the quality of this manuscript. We also would like to thank Sharon Lackie, Electron Microscope Technician at the University of Windsor for her help in obtaining the SEM images presented in this manuscript.

**Conflicts of Interest:** The authors declare no conflict of interest.

## References

- European Patent Office. *Innovation Trends in Additive Manufacturing Patents in 3D Printing Technologies*; European Patent Office: Munich, Germany, 2023; Available online: <https://link.epo.org/web/service-support/publications/en-additive-manufacturing-study-2023-full-study.pdf> (accessed on 3 March 2024).
- Boyer, R.R. Titanium for aerospace: Rationale and applications. *Adv. Perform. Mater.* **1995**, *2*, 349–368. [[CrossRef](#)]
- Gialanella, S.; Malandrucolo, A. *Aerospace Alloys*; Springer International Publishing: Cham, Switzerland, 2020.
- Brewer, W.D.; Bird, R.; Wallace, T.A. Titanium alloys and processing for high speed aircraft. *Mater. Sci. Eng. A* **1998**, *243*, 299–304. [[CrossRef](#)]
- Cotton, J.D.; Clark, L.P.; Phelps, H.R. Titanium alloys on the F-22 fighter airframe. *Adv. Mater. Process.* **2002**, *160*, 25–28.
- Saito, T. The automotive application of discontinuously reinforced TiB-Ti composites. *JOM* **2004**, *56*, 33–36. [[CrossRef](#)]
- Hanusiak, W.; Fields, J.; Hammond, V.; Grabow, R.; Yolton, C.F. The prospects for hybrid fiber-reinforced Ti-TiB-matrix composites. *JOM* **2004**, *56*, 49–50. [[CrossRef](#)]
- Fereiduni, E.; Ghasemi, A.; Elbestawi, M. Selective Laser Melting of Aluminum and Titanium Matrix Composites: Recent Progress and Potential Applications in the Aerospace Industry. *Aerospace* **2020**, *7*, 77. [[CrossRef](#)]
- Lomo, F.; Vargas-Uscategui, A.; King, P.; Patel, M.; Cole, I. Microstructure and mechanical properties of heat-treated cold spray additively manufactured titanium metal matrix composites. *J. Manuf. Process.* **2023**, *99*, 12–26. [[CrossRef](#)]
- Fang, M.; Han, Y.; Shi, Z.; Huang, G.; Song, J.; Lu, W. Embedding boron into Ti powder for direct laser deposited titanium matrix composite: Microstructure evolution and the role of nano-TiB network structure. *Compos. Part B Eng.* **2021**, *211*, 108683. [[CrossRef](#)]
- Macke, A.; Schultz, B.; Rohatgi, P. Metal Matrix Composites Offer Automotive Industry Opportunity to Reduce Vehicle Weight, Improve Performance. *AMP Tech. Artic.* **2012**, *170*, 19–23. [[CrossRef](#)]
- Miracle, D. Metal matrix composites—From science to technological significance. *Compos. Sci. Technol.* **2005**, *65*, 2526–2540. [[CrossRef](#)]
- Hooker, J.; Doorbar, P. Metal matrix composites for aeroengines. *Mater. Sci. Technol.* **2000**, *16*, 725–731. [[CrossRef](#)]
- Hayat, M.D.; Singh, H.; He, Z.; Cao, P. Titanium metal matrix composites: An overview. *Compos. Part A Appl. Sci. Manuf.* **2019**, *121*, 418–438. [[CrossRef](#)]
- Ammisetti, D.K.; Kruthiventi, S.S.H. Recent trends on titanium metal matrix composites: A review. *Mater. Today Proc.* **2020**, *46*, 9730–9735. [[CrossRef](#)]
- Singh, G.; Ramamurty, U. Boron modified titanium alloys. *Prog. Mater. Sci.* **2020**, *111*, 100653. [[CrossRef](#)]

17. Li, Q.; Huang, S.; Zhao, Y.; Gao, Y.; Ramamurty, U. Simultaneous enhancements of strength, ductility, and toughness in a TiB reinforced titanium matrix composite. *Acta Mater.* **2023**, *254*. [[CrossRef](#)]
18. Li, S.; Wang, X.; Le, J.; Han, Y.; Zong, N.; Wei, Z.; Huang, G.; Lu, W. Towards high strengthening efficiency by in-situ planting nano-TiB networks into titanium matrix composites. *Compos. Part B Eng.* **2022**, *245*, 110169. [[CrossRef](#)]
19. Zhang, T.; Liu, C.-T. Design of titanium alloys by additive manufacturing: A critical review. *Adv. Powder Mater.* **2021**, *1*, 100014. [[CrossRef](#)]
20. Liu, Z.; He, B.; Lyu, T.; Zou, Y. A Review on Additive Manufacturing of Titanium Alloys for Aerospace Applications: Directed Energy Deposition and Beyond Ti-6Al-4V. *JOM* **2021**, *73*, 1804–1818. [[CrossRef](#)]
21. Moghimian, P.; Poirié, T.; Habibnejad-Korayem, M.; Zavala, J.A.; Kroeger, J.; Marion, F.; Larouche, F. Metal powders in additive manufacturing: A review on reusability and recyclability of common titanium, nickel and aluminum alloys. *Addit. Manuf.* **2021**, *43*, 102017. [[CrossRef](#)]
22. Kumar, M.B.; Sathiya, P. Methods and materials for additive manufacturing: A critical review on advancements and challenges. *Thin-Walled Struct.* **2020**, *159*, 107228. [[CrossRef](#)]
23. Charmi, A.; Falkenberg, R.; Ávila, L.; Mohr, G.; Sommer, K.; Ulbricht, A.; Sprengel, M.; Neumann, R.S.; Skrotzki, B.; Evans, A. Mechanical anisotropy of additively manufactured stainless steel 316L: An experimental and numerical study. *Mater. Sci. Eng. A* **2020**, *799*, 140154. [[CrossRef](#)]
24. Ren, Y.; Tariq, N.U.H.; Liu, H.; Zhao, L.; Cui, X.; Shen, Y.; Wang, J.; Xiong, T. Study of microstructural and mechanical anisotropy of 7075 Al deposits fabricated by cold spray additive manufacturing. *Mater. Des.* **2021**, *212*, 110271. [[CrossRef](#)]
25. Kok, Y.; Tan, X.; Wang, P.; Nai, M.; Loh, N.; Liu, E.; Tor, S. Anisotropy and heterogeneity of microstructure and mechanical properties in metal additive manufacturing: A critical review. *Mater. Des.* **2018**, *139*, 565–586. [[CrossRef](#)]
26. Chang, K.; Liang, E.; Huang, W.; Zhang, X.; Chen, Y.; Dong, J.; Zhang, R. Microstructural feature and mechanical property in different building directions of additive manufactured Ti6Al4V alloy. *Mater. Lett.* **2020**, *267*, 127516. [[CrossRef](#)]
27. Sun, W.; Ma, Y.; Huang, W.; Zhang, W.; Qian, X. Effects of build direction on tensile and fatigue performance of selective laser melting Ti6Al4V titanium alloy. *Int. J. Fatigue* **2019**, *130*, 105260. [[CrossRef](#)]
28. Edwards, P.; Ramulu, M. Fatigue performance evaluation of selective laser melted Ti-6Al-4V. *Mater. Sci. Eng. A* **2014**, *598*, 327–337. [[CrossRef](#)]
29. Tang, D.; He, X.; Wu, B.; Dang, L.; Xin, H.; Li, Y. Anisotropic fatigue performance of directed energy deposited Ti-6Al-4V: Effects of build orientation. *Mater. Sci. Eng. A* **2023**, *876*, 145112. [[CrossRef](#)]
30. Samandi, M.; Storm, R.; Loutfy, R.; Withers, J. The Development of Plasma Transferred Arc Solid Free Form Fabrication as a Cost Effective Production Methodology. In Proceedings of the 22nd Heat Treating Society Conference and the 2nd International Surface Engineering Congress, Indianapolis, IN, USA, 15–17 September 2003; pp. 513–518.
31. Balakumar, T.; Riahi, R.; Edrisy, A. An investigation of fatigue of additively manufactured commercially pure Alpha-Ti alloy at 350 °C. *J. Mater. Res. Technol.* **2023**, *26*, 7300–7311. [[CrossRef](#)]
32. Sangid, M.D. The physics of fatigue crack initiation. *Int. J. Fatigue* **2013**, *57*, 58–72. [[CrossRef](#)]
33. Arakawa, J.; Kawahara, Y.; Kimura, Y.; Hashimoto, S.; Akebono, H.; Sugeta, A. Estimation of the fatigue crack initiation site and life of Ti-6Al-4V alloy for two types of circle and slender crystal grains. *Int. J. Fatigue* **2024**, *181*, 108097. [[CrossRef](#)]
34. Meng, F.; Zhang, R.; Wang, S.; Sun, F.; Chen, R.; Huang, L.; Geng, L. Fatigue Crack Initiation and Propagation Dominated by Crystallographic Factors in TiB/near  $\alpha$ -Ti Composite. *Acta Met. Sin.* **2024**. [[CrossRef](#)]

**Disclaimer/Publisher’s Note:** The statements, opinions and data contained in all publications are solely those of the individual author(s) and contributor(s) and not of MDPI and/or the editor(s). MDPI and/or the editor(s) disclaim responsibility for any injury to people or property resulting from any ideas, methods, instructions or products referred to in the content.